Supplementary Information

Lattice-Coherent Epitaxial Surface Engineering in Highly Stable Co-Free Ultrahigh-Ni Cathodes

Fuqiren Guo[a], Liangchi Yang[a], Shuli Zheng[a], Xianyan Qiao[a], Heng Zhang[b], Yong Ming[c], Fang Wan[a], Zhenguo Wu[a], Lang Qiu[a, *], Xiaodong Guo[a, *]

a School of Chemical Engineering, Sichuan University, Chengdu 610065, PR China.

b School of Materials Science and Engineering, Suzhou University of Science and Technology, Suzhou 215009, PR China.

c School of Chemical Engineering, Sungkyunkwan University, Suwon 16419, South Korea.

** Corresponding authors.*

** E-mail addresses: qiulang2023@scu.edu.cn (Lang Qiu)*

** E-mail addresses: xiaodong2009@scu.edu.com (Xiaodong Guo)*

Experimental Section

Material Synthesis

The Mn-rich shell $Ni_{0.95}Al_{0.05}(OH)_2$ precursors and pristine hydroxide were all prepared via the co-precipitation method in a batch-type reactor of 20 L with reaction time of 40 h, denoted as VCS-NMA and C-NMA, respectively. For the precursor of C-NMA, a 1.9 M transition metal sulfate aqueous solution of stoichiometric mole ratio mixed $NiSO_4 \cdot 6H_2O$ and $MnSO_4 \cdot H_2O$ was pumped into the reactor under Ar atmosphere. Then 4 M sodium hydroxide solution and 2.4 M ammonia solution were pumped simultaneously through a peristaltic pump. Sodium aluminate ($NaAlO_2$) as aluminum salt (0.1 M) was added to the ammonia solution for feeding. For the VCS-NMA precursor, which consists of $Ni_{0.95}Al_{0.05}(OH)_2$ in the particle core and $Ni_{0.75}Mn_{0.2}Al_{0.05}(OH)_2$ on the particle surface, a starting 1.9 M solution mixture of $NiSO_4 \cdot 6H_2O$ was firstly pumped in to the reactor first for 30 h, and then the other 1.9 M solution mixture of $NiSO_4 \cdot 6H_2O$ and $MnSO_4 \cdot H_2O$ were pumped in to the reactor for 10 h. The feed conditions for sodium hydroxide solution, ammonia solution, and sodium aluminate were identical to those employed for C-NMA. The pH value (11.0 ± 0.1), temperature (50 ± 0.2 °C), and stirring speed (700 rpm) were carefully controlled, and the whole process was carried out in an Ar atmosphere. Finally, two precursors were filtered, washed, and dried. Two kinds of $LiNi_{0.9}Mn_{0.05}Al_{0.05}O_2$ cathode materials were prepared by calcining appropriate amounts of the precursors and $LiOH \cdot H_2O$ at 750 °C for 15 h in O_2.

Electrochemical Measurements

The active material, carbon black, and polyvinylidene fluoride (PVDF) were blended in *n*-methyl-2-pyrrolidone (NMP) solvent with a mass ratio of 80 : 13 : 7 to fabricate the electrode slurry. The slurry was coated on Al foil with the active material loading of approximately 3.5 ± 0.2 mg cm^{-2} and dried under vacuum at 120 ℃. The 2025 coin-type cells were assembled in an argon-filled glove box (the contents of both O_2 and H_2O were ≤ 0.1 ppm) using lithium tablet, polyethylene, and 1M $LiPF_6$ in ethyl carbonate/dimethyl carbonate/diethyl carbonate (EC : DMC : DEC=1 : 1 : 1 by volume)

as the anode, separator, and electrolyte, respectively. The charge/discharge measurements were performed through the NEWARE CT-4008 battery-testing system within a voltage range of 2.7-4.4 V (*vs*. Li/Li^+, 1 C=180 mA g^{-1}) at 25 °C under constant current and constant voltage modes. Electrochemical impedance spectroscopy (EIS) measurements were executed on an electrochemical workstation (Zennium IM6) with an amplitude of 5 mV over the frequency ranging from 100 kHz to 0.01 Hz. Galvanostatic intermittent titration technique (GITT) were carried with magnitudes of 18 mA g^{-1} for 10 min, followed by 60 min relaxation.

Material Characterizations

The crystalline structure of all samples was characterized by X-ray diffraction (XRD, Cu Kα radiation, Bruker D8 Advance, scanning range 10-80°, scan speed 3.5° min^{-1}). The collected data of XRD were analyzed by applying the GSAS Rietveld refinement program. The morphology, microstructure, and element distribution of the samples were characterized by scanning electron microscope (SEM, ZEISS Gemini 300), transmission electron microscopy (TEM, FEI Tecnai G20), and energy dispersive spectrometry (EDS). Cross-sectional SEM and TEM of the cathode particles were prepared through a focused ion beam technology (FIB, FEI Tecnai G20). Spherical aberration corrected transmission electron microscope (STEM) with electron energy loss spectroscopy (EELS) configuration was used to detect atomic-scale microstructure and electronic structure of element (Thermalfisher scientific titan themsis Z). The chemical compositions were identified by Inductively Coupled Plasma Mass Spectrometry (ICP, OPTIMA 7000 DV, PerkinElmer). The in-situ high-termperature XRD (HR-XRD, heating range 25-900 ℃, heating rate 10 ℃ min^{-1}, oxygen atmosphere) were used to analyze the phase evolution of precursor mixtures of $TM(OH)_2$ and LiOH. The in-situ high-termperature XRD (HR-XRD, heating range 20-600 ℃, heating rate 10 ℃ min^{-1}, Ar atmosphere without electrolyte) were used to analyze the thermal stability of the samples. Electron paramagnetic resonance (EPR, JEOL JES-FA200) was used for the detection of oxygen vacancies (unpaired electron paramagnetic materials). The cross-sectional characterization of particles after cycle was performed using a JEOL CP (Ion Cross Section Polisher, IB-09020CP). The time-

of-flight secondary ion mass spectrometry (TOF-SIMS, ION-TOF TOF. SIMS5) depth profiling of both cycled cathodes was used to analyze the cathode-electrolyte interphase films.

Supplementary Figure

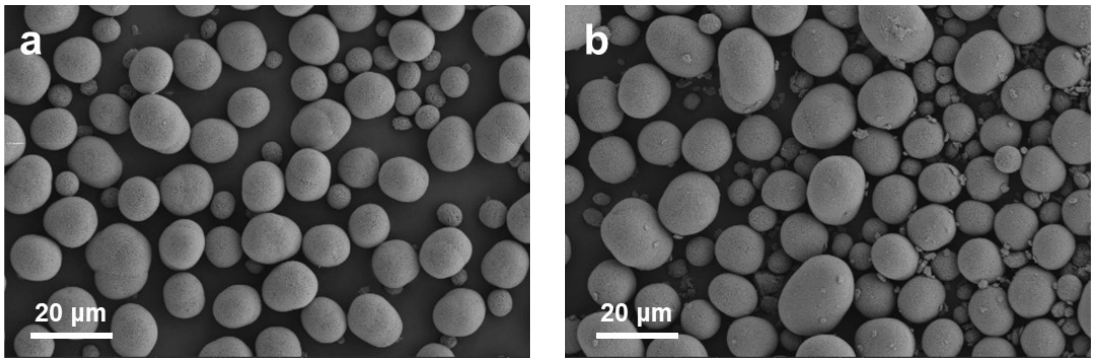

Fig. S1 SEM images of precursor for (a) C-NMA and (b) VCS-NMA. It illustrates a similar size distribution of primary and secondary particles.

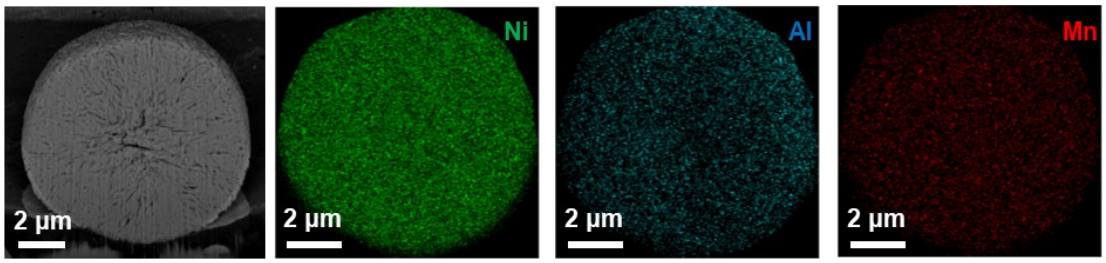

Fig. S2 Cross-sectional FIB-SEM and EDS mapping images of C-NMA precursor.

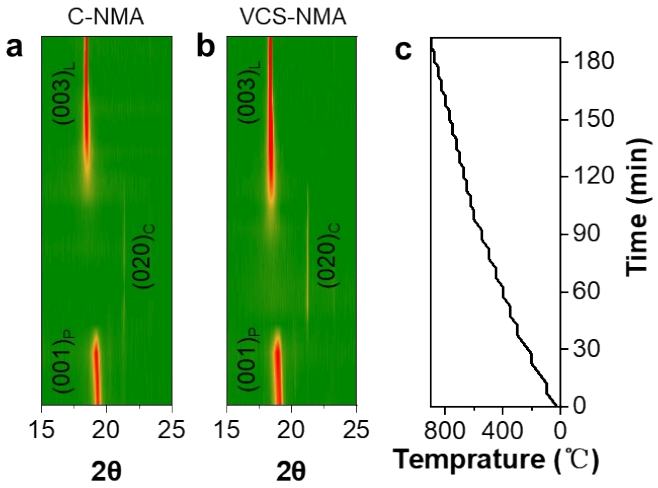

Fig. S3 The enlarged version of the $(003)_L$ peaks evolution of (a) C-NMA and (b) VCS-NMA during oxygen-rich environment, with the corresponding temperature curves aligned to the left (c).

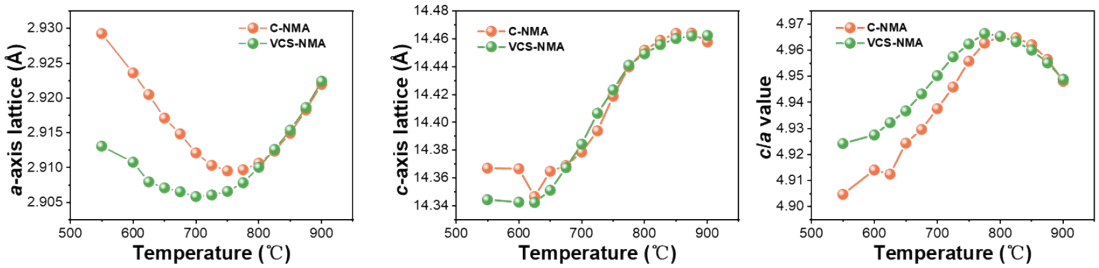

Fig. S4 The evolution of the corresponding (a) *a*-axis parameter, (b) *c*-axis parameter, and (c) calculated *c*/*a* values for C-NMA and VCS-NMA during oxygen-rich environment.

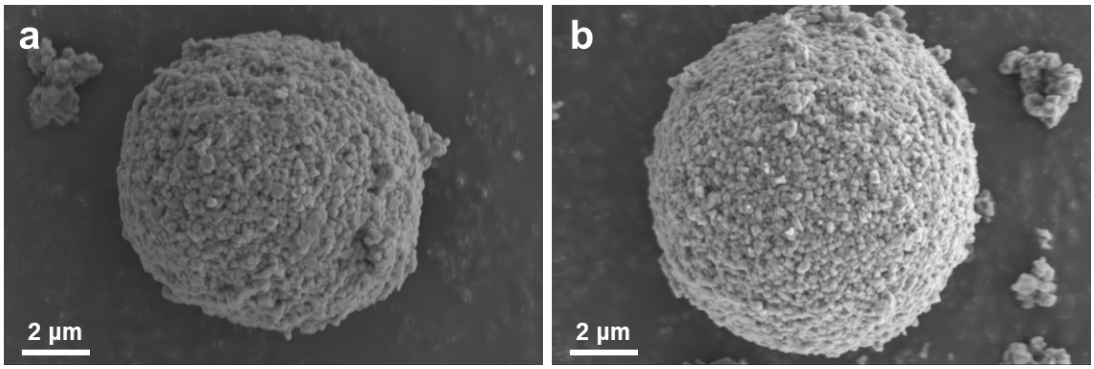

Fig. S5 SEM images of (a) C-NMA and (b) VCS-NMA.

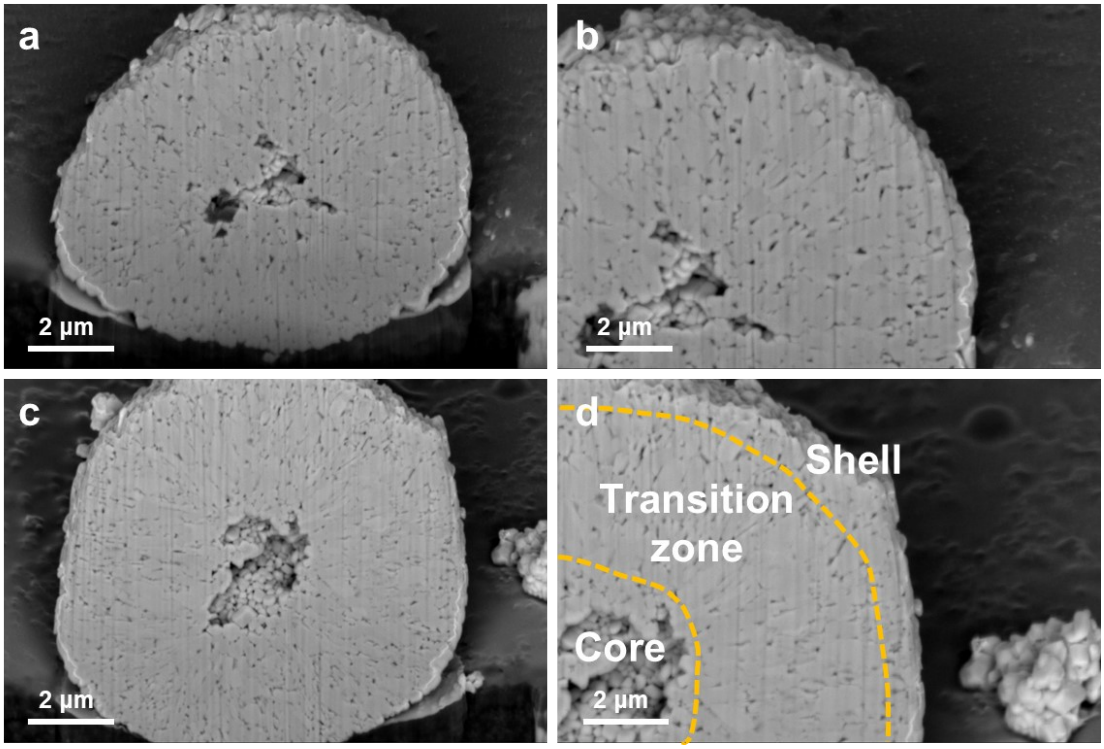

Fig. S6 Cross-sectional FIB-SEM images of (a-b) C-NMA and (c-d) VCS-NMA.

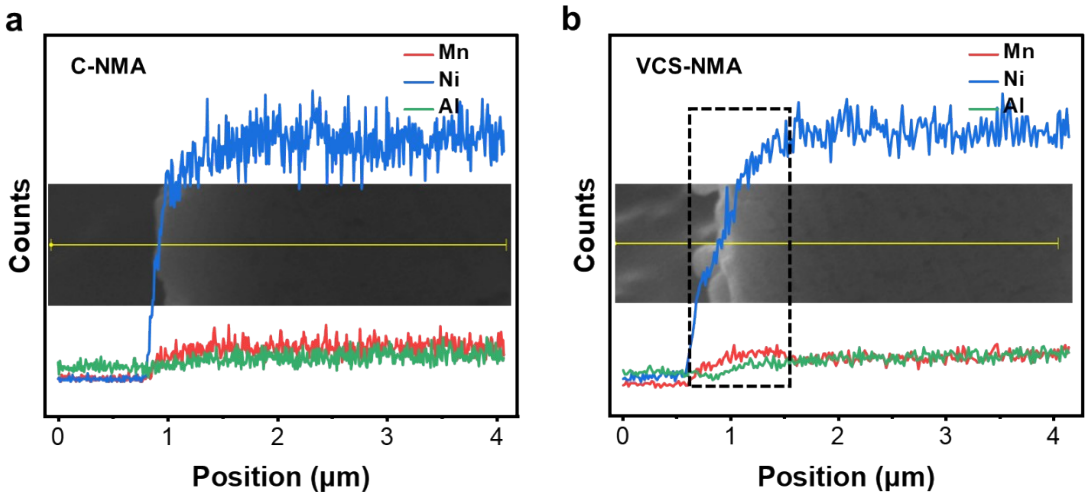

Fig. S7 The EDS line scanning of (a) C-NMA and (b) VCS-NMA with corresponding cross-sectional SEM images.

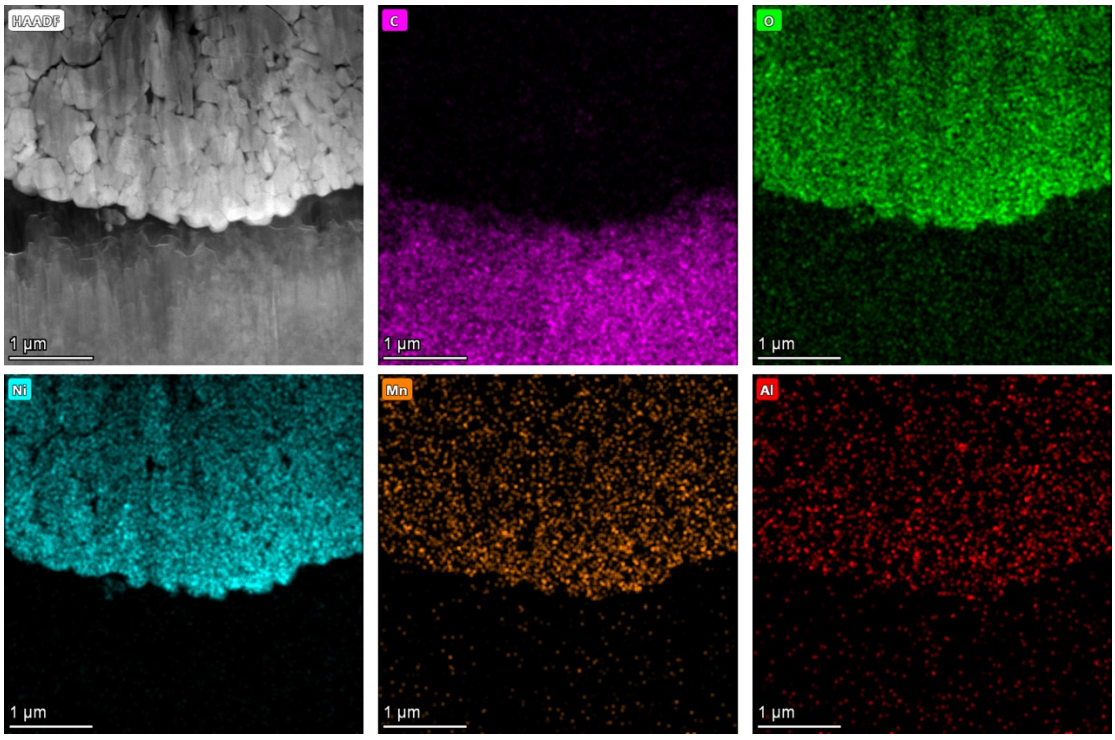

Fig. S8 Cross-sectional HAADF images for C-NMA with EDS mapping images.

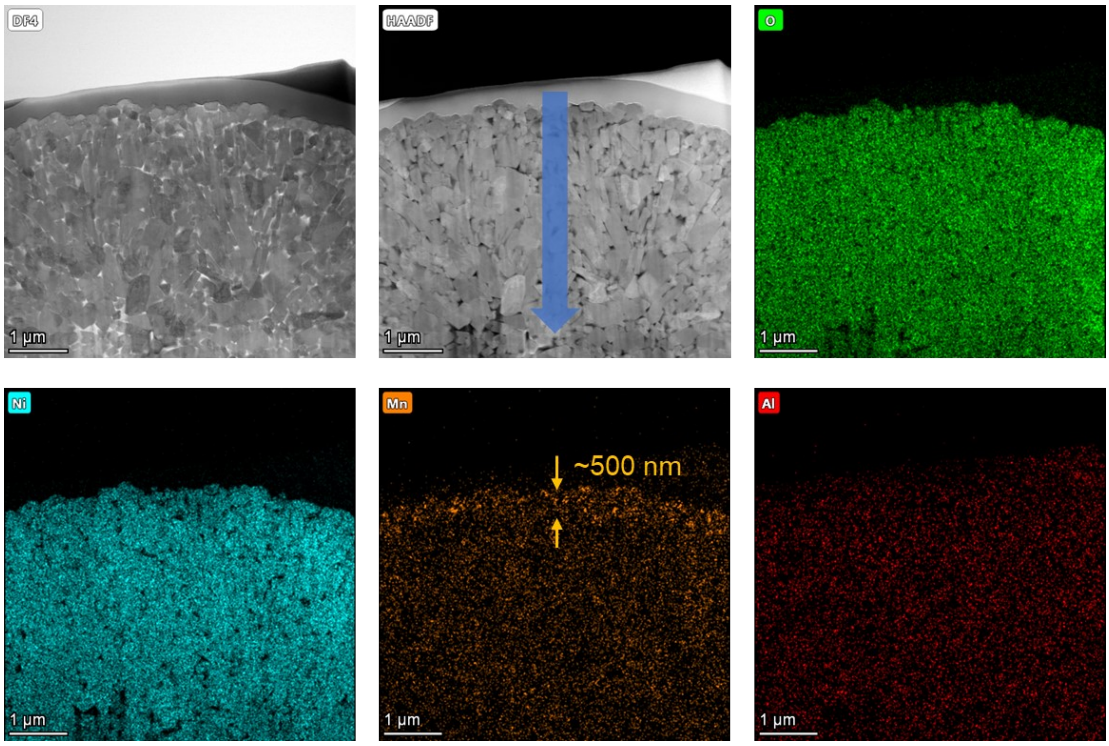

Fig. S9 Cross-sectional HAADF images for VCS-NMA with EDS mapping images, and the EELS line-scan pathway for Fig. 1h is indicated by blue arrow.

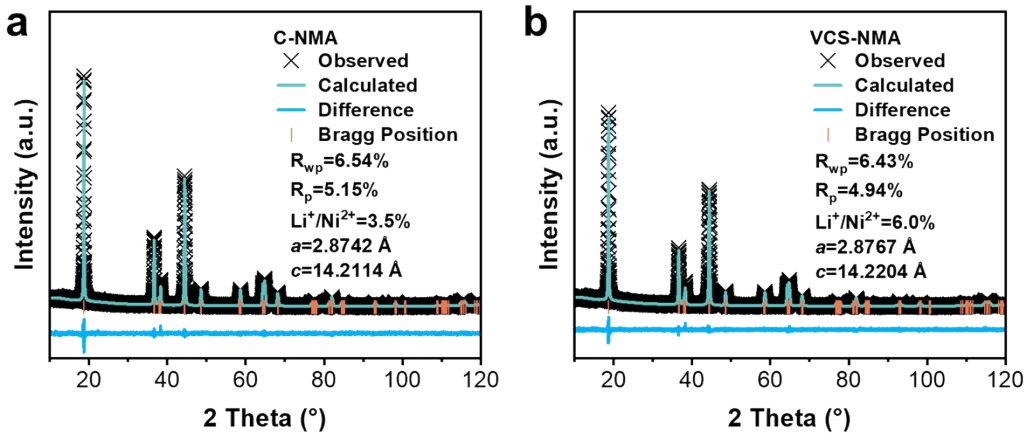

Fig. S10 Refined XRD patterns of (a) C-NMA and (b) VCS-NMA.

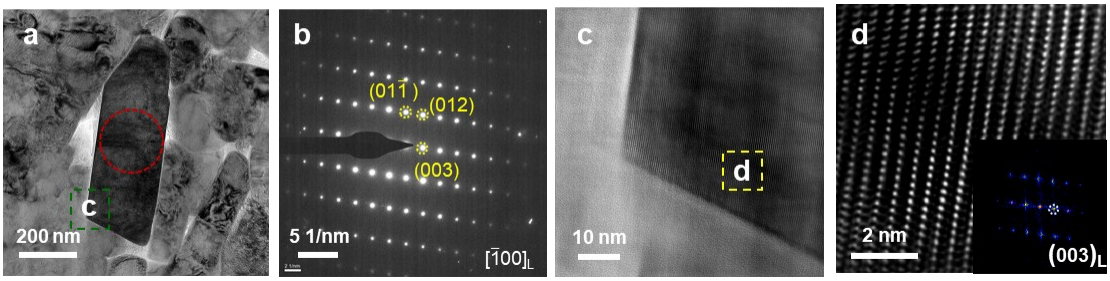

Fig. S11 (a) ABF images of primary particle located inside the secondary particle (site S1 in Fig. 2n) for C-NMA. (b) SAED pattern of the region marked by red dotted cycle region in (a). (c-d) HR-TEM images and corresponding fast Fourier transforms of the primary particle located inside the secondary particle for C-NMA.

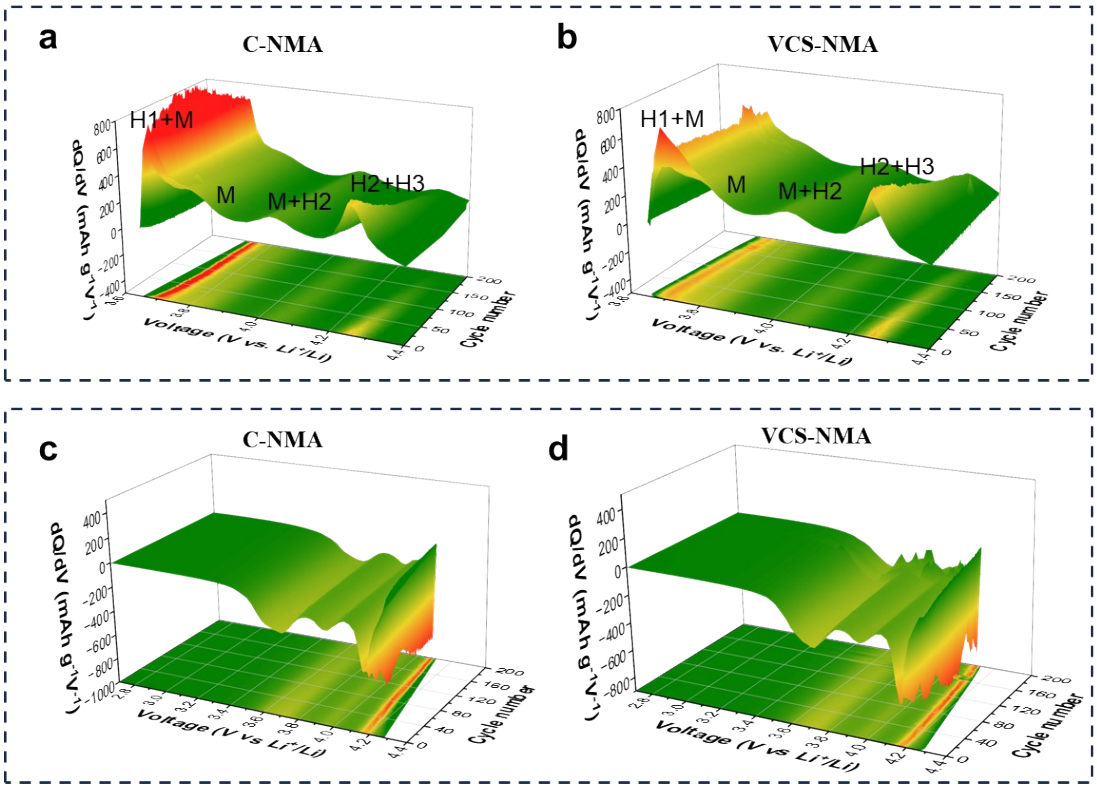

Fig. S12 The dQ/dV curves of (a-b) charge and (c-d) discharge for C-NMA and VCS-NMA.

The reversibility of the phase transition can be intuitively evaluated via the redox peaks in dQ/dV curves, including hexagonal to monoclinic (H1-M at ≈ 3.7 V) phase transition, monoclinic to hexagonal (M-H2 at ≈ 4.0 V) phase transition, and hexagonal to hexagonal (H2-H3 at ≈ 4.2 V) phase transition.[1]

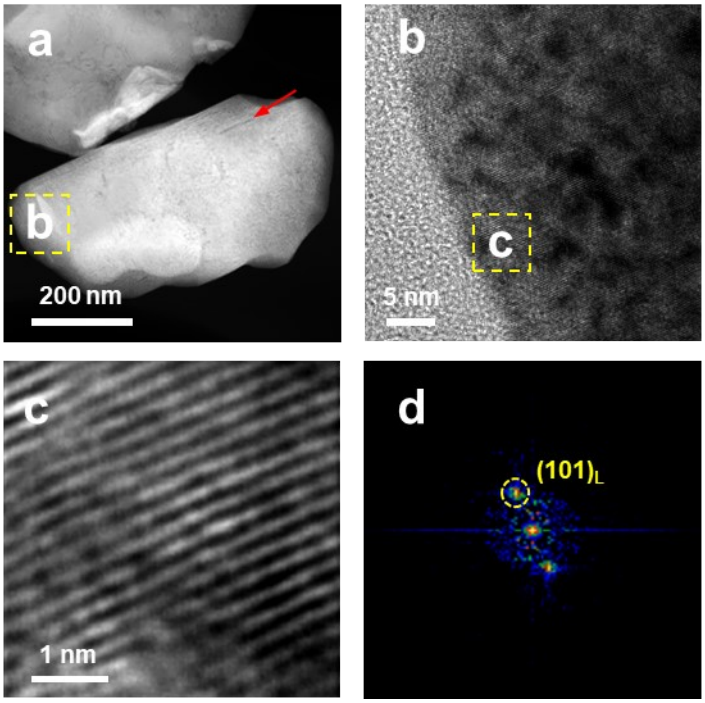

Fig. S13 (a) Low-magnification HAAD images, (b) TEM images, and FFT images of VCS-NMA at charging 4.4 V.

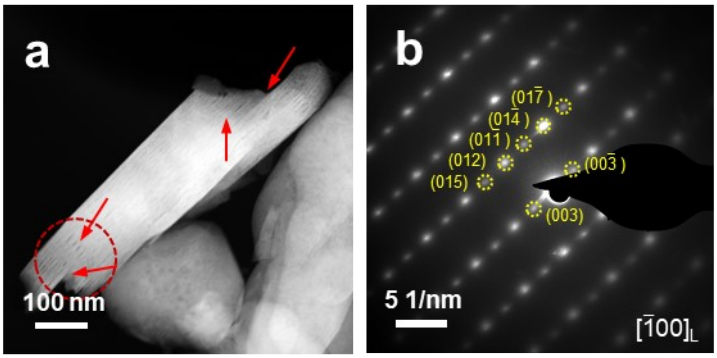

Fig. S14 (a) Low-magnification HAAD images and (b) SAED pattern of C-NMA at charging 4.4 V, and the intragranular cracks are marked by red arrows.

The SAED pattern recorded along the [-100] zone axis of a primary particle of C-NMA cathode at charging 4.4 V displays elongated diffraction spots in the *c*-direction, indicating narrow regions with stacking faults and misaligned Li and TM layers.[2]

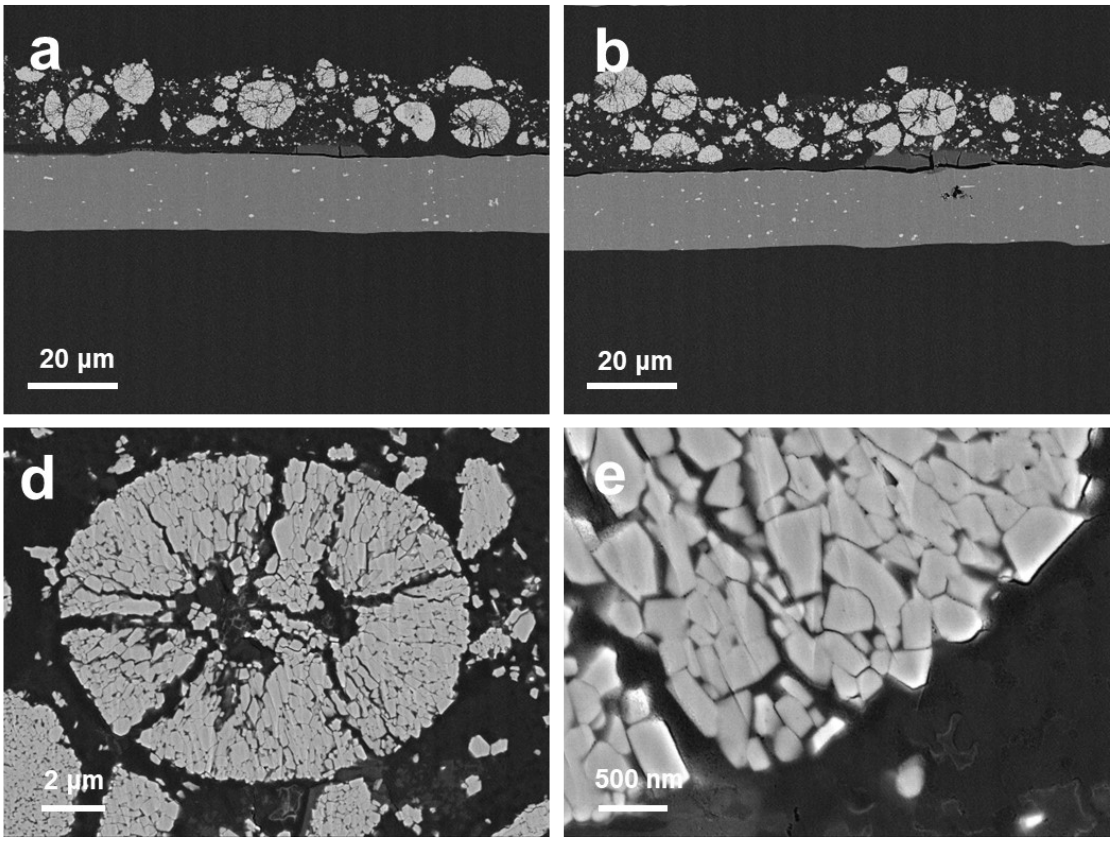

Fig. S15 Cross-sectional FIB-SEM images of C-NMA after 200 cycles.

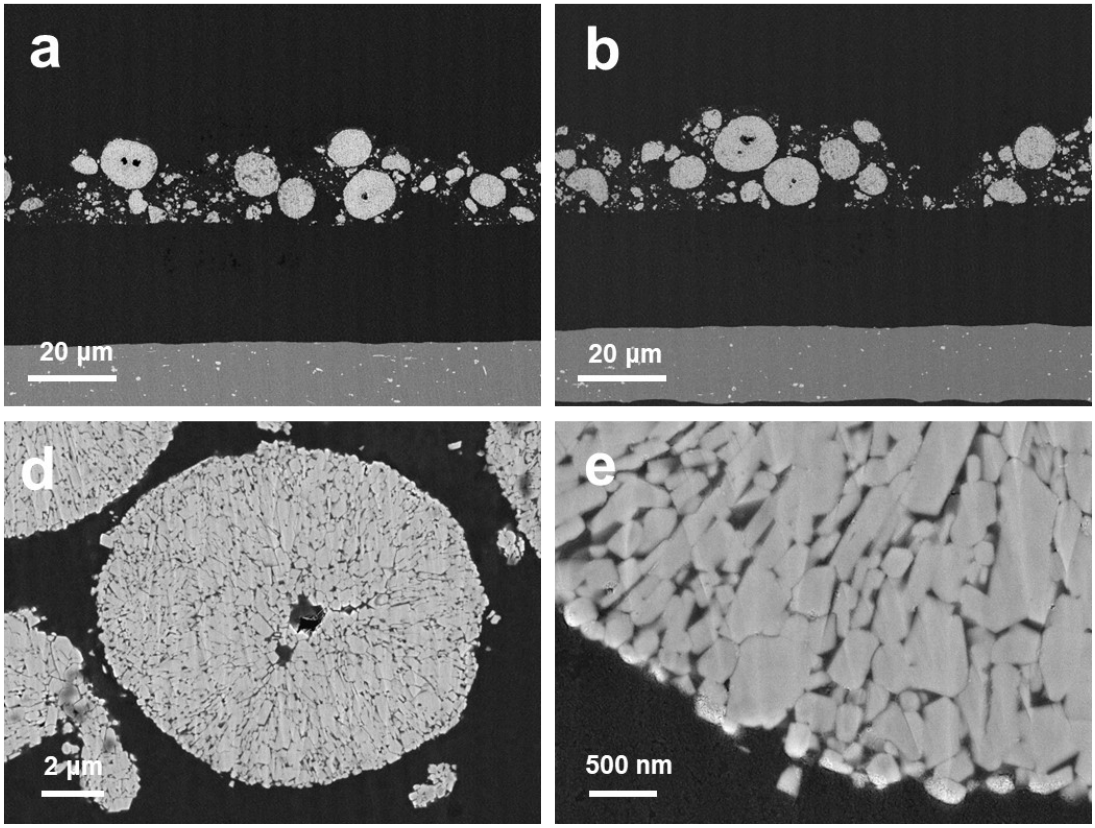

Fig. S16 Cross-sectional FIB-SEM images of VCS-NMA after 200 cycles.

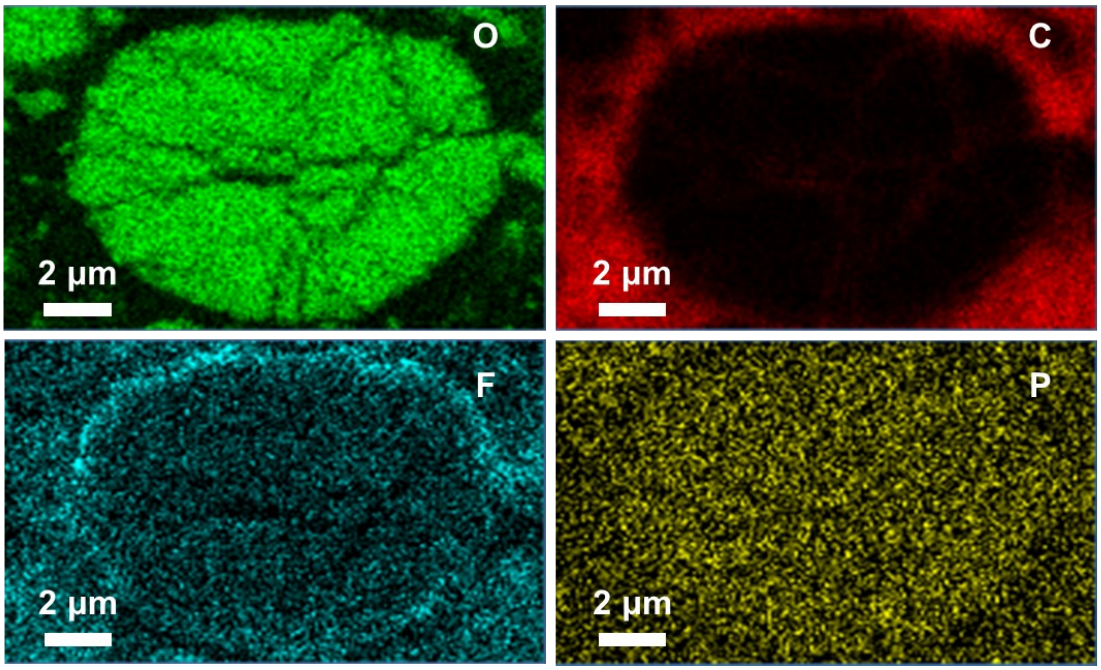

Fig. S17 Cross-sectional FIB-SEM EDS mapping images of C-NMA after 200 cycles.

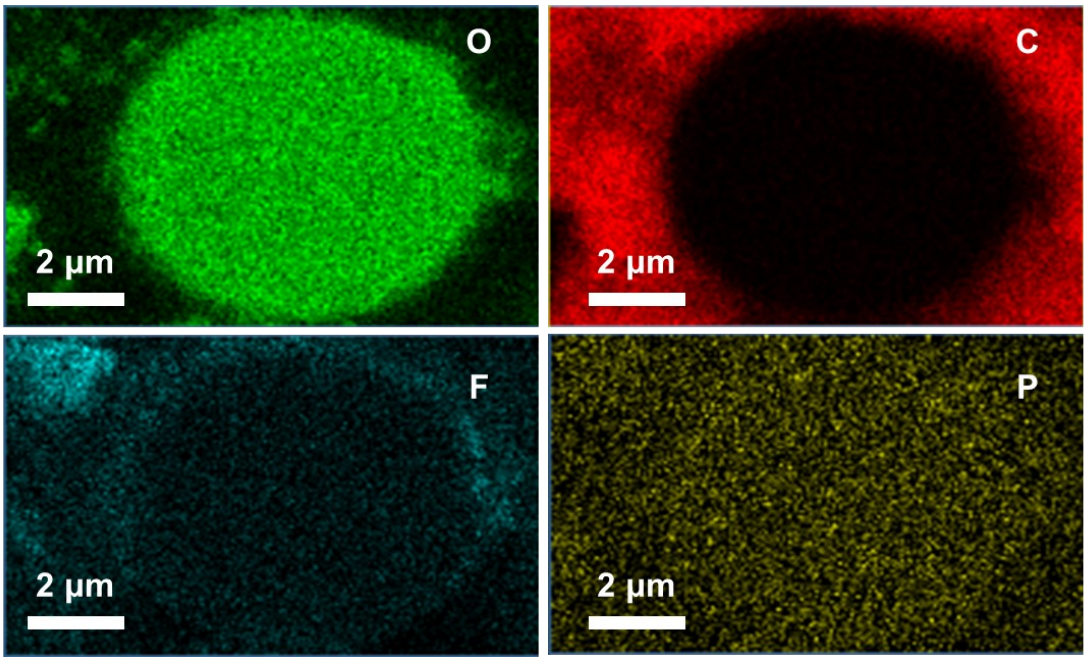

Fig. S18 Cross-sectional FIB-SEM EDS mapping images of VCS-NMA after 200 cycles.

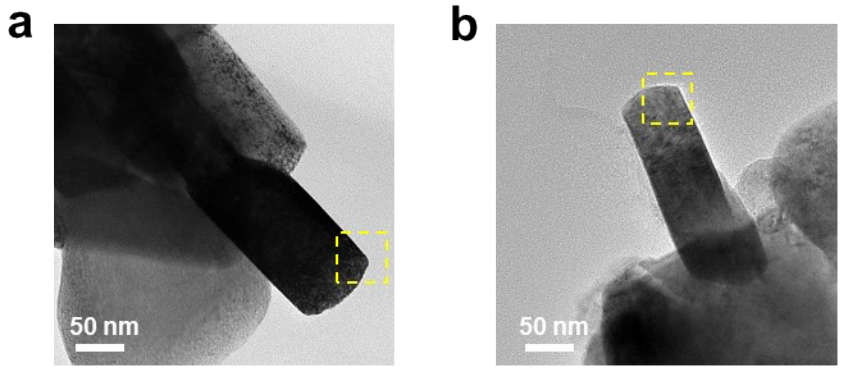

Fig. S19 Low-magnification TEM images of (a) C-NMA and (b) VCS-NMA after 200 cycles.

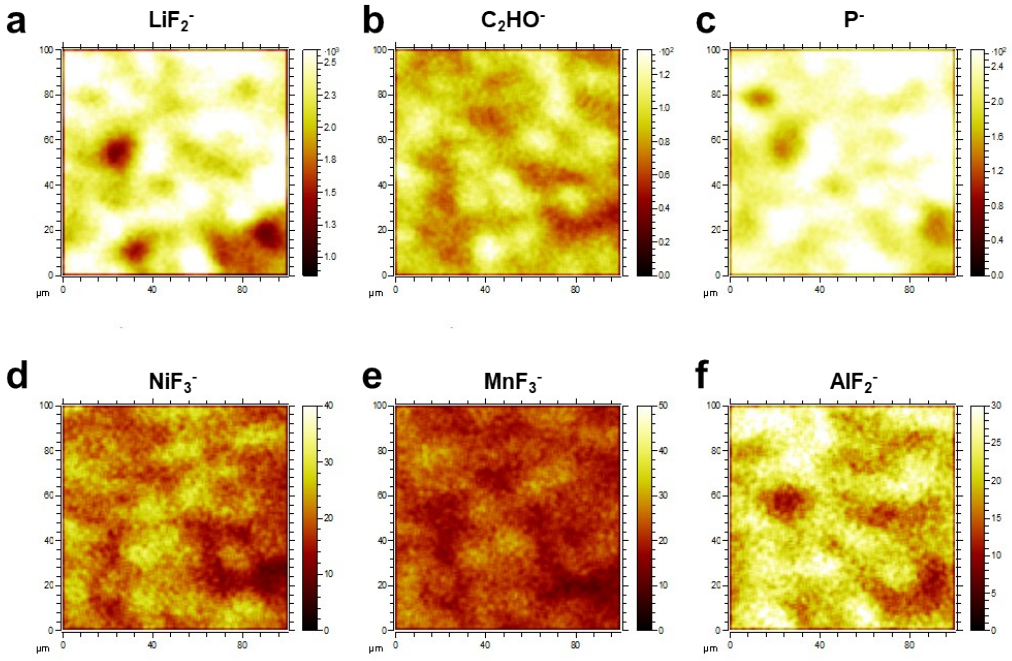

Fig. S20 TOF-SIMS mapping images of C-NMA after 200 cycles.

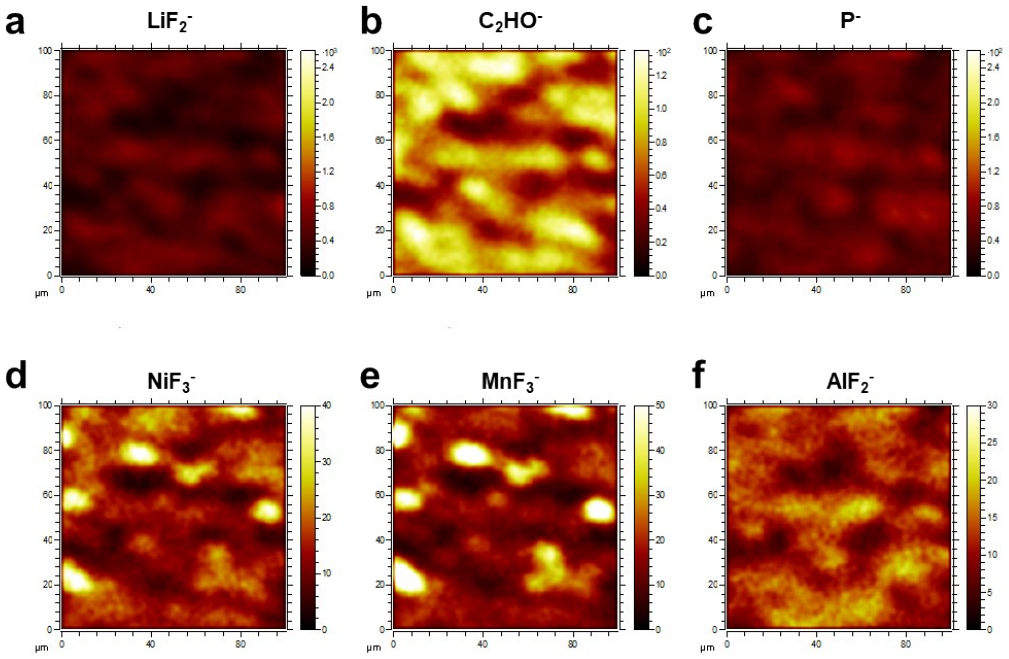

Fig. S21 TOF-SIMS mapping images of VCS-NMA after 200 cycles.

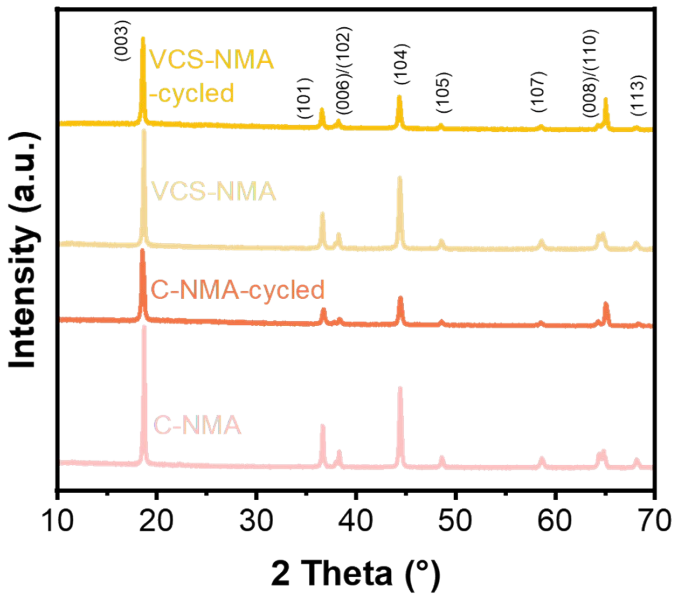

Fig. S22 XRD patterns of C-NMA and VCS-NMA.

Supplementary Table

Table. S1 Element composition of C-NMA and VCS-NMA precursor. The composition of three precursors is in accordance with the design expectation.

Samples	Ni (mol %)	Mn (mol %)	Al (mol %)
C-NMA	89.796	5.288	4.916
VCS-NMA	90.375	5.313	4.312

Table. S2 Rietveld refinement results of XRD data for C-NMA sample (Chi^2 = 1.429).

Sample	$I_{(003)}/I_{(104)}$	*a*(Å)	*c*(Å)	Volume(Å^3)	Site		*x*	*y*	*z*	Occupancy	R_{wp} (%)	R_p (%)
					Li	3a	0	0	0	0.965(1)		
					Ni	3a	0	0	0	0.035(1)		
					Ni	3b	0	0	0.5	0.865(1)		
C-NMA	1.75	2.8742(0)	14.2114(2)	101.671(2)	Li	3b	0	0	0.5	0.035(1)	6.54	5.15
					Mn	3b	0	0	0.5	0.100		
					Al	3b	0	0	0.5	0.100		
					O	6c	0	0	0.2406(1)	1.000		

Table. S3 Rietveld refinement results of XRD data for VCS-NMA sample (Chi^2=1.390).

Sample	$I_{(003)}/I_{(104)}$	*a*(Å)	*c*(Å)	Volume(Å^3)	Site		*x*	*y*	*z*	Occupancy	R_{wp} (%)	R_p (%)
VCS-NMA	1.64	2.8767(0)	14.2203(3)	101.910(3)	Li	3a	0	0	0	0.940(1)	6.43	5.06
					Ni	3a	0	0	0	0.060(1)		
					Ni	3b	0	0	0.5	0.840(1)		
					Li	3b	0	0	0.5	0.060(1)		
					Mn	3b	0	0	0.5	0.050		
					Al	3b	0	0	0.5	0.050		
					O	6c	0	0	0.2598(1)	1.000		

Table. S4 The fitted EIS results of C-NMA and VCS-NMA cathodes after 200 cycles. Although similar surface film impedance (R_s) is exhibited for three cathodes (12.4 Ω for C-NMA and 9.7 Ω for VCS-NMA, the charge transfer impedance (R_{ct}) of C-NMA is 350.0 Ω, which is 29.5% higher than that of VCS-NMA (270.3 Ω).

/	C-NMA	VCS-NMA
R_s (Ω)	12.4	9.7
R_{ct} (Ω)	350.0	270.3

Reference

1. F. Guo, Y. Hu, Z. Zeng, X. Qiao, H. Yang, Q. Chen, H. Li, Z. Li, L. Qiu, Z. Wu, Y. Song and X. Guo, *Energy Storage Materials*, 2024, **71**, 103641.
2. G.-T. Park, D. R. Yoon, U.-H. Kim, B. Namkoong, J. Lee, M. M. Wang, A. C. Lee, X. W. Gu, W. C. Chueh, C. S. Yoon and Y.-K. Sun, *Energy & Environmental Science*, 2021, **14**, 6616-6626.